

## RESEARCH ARTICLE OPEN ACCESS

# Validation of qMT and CEST MRI as Biomarkers of Response to Treatment After Lumbar Spinal Cord Injury in Rats

Chaoqi Mu<sup>1,2,3</sup>  | Jamie L. Reed<sup>1,2</sup> | Feng Wang<sup>1,2</sup>  | Xinqiang Yan<sup>1,2</sup> | Ming Lu<sup>1,2</sup> | John C. Gore<sup>1,2,3</sup> | Li Min Chen<sup>1,2,3</sup>

<sup>1</sup>Vanderbilt University Institute of Imaging Science, Vanderbilt University, Nashville, Tennessee, USA | <sup>2</sup>Department of Radiology and Radiological Sciences, Vanderbilt University Medical Center, Nashville, Tennessee, USA | <sup>3</sup>Department of Biomedical Engineering, Vanderbilt University, Nashville, Tennessee, USA

**Correspondence:** Li Min Chen ([limin.chen@vanderbilt.edu](mailto:limin.chen@vanderbilt.edu))

**Received:** 11 December 2024 | **Revised:** 30 January 2025 | **Accepted:** 6 February 2025

**Funding:** This study is supported by the U.S. Department of Defense (DOD) Grant SC190134 (awarded to Li Min Chen) and the National Institute of Neurological Disorders and Stroke, National Institutes of Health (NIH) Grant F31 NS113949 (awarded to Chaoqi Mu) and acknowledges the support also of NIH award 1S10OD025085 (awarded to John C. Gore). We acknowledge additional NIH support for instrumentation, 1S10OD016245-01 and 1S10RR023784-01, from the Office of Research Infrastructure Programs, National Institutes of Health.

**Keywords:** chemical exchange saturation transfer (CEST) | imaging biomarker | MRI | neuroprotective treatment | preclinical imaging | quantitative magnetization transfer (qMT) | spinal cord injury

## ABSTRACT

The progression and repair of a traumatically injured spinal cord (SCI) involves multifaceted processes. Noninvasive, mechanism-informative objective biomarkers could greatly facilitate the translation of findings from preclinical animal models to patient applications. We aimed to develop and validate multiparametric chemical exchange saturation transfer (CEST) and quantitative magnetization transfer (qMT) magnetic resonance imaging (MRI) biomarkers for assessing SCI severity, demyelination, and neuroinflammation, as well as the response to neuroprotective drug treatment riluzole. Changes in CEST and qMT MRI metrics before and after a moderate contusion injury at the L1 level of the lumbar spinal cord were compared between two groups of rats that received either the riluzole or a vehicle treatment over 8 weeks. The specificity of these MRI biomarkers was validated by postmortem immunohistology. The functional relevance of these biomarkers was evaluated by correlation with hindlimb sensorimotor and pain behavior. The pool size ratio (PSR) maps from qMT acquisitions of the SCI region in riluzole-treated rats showed increased white matter macromolecular content compared to the HBC vehicle-treated group, suggesting increased myelin levels and possible remyelination of the injured spinal cord. CEST APT pool (3.5 ppm) amplitude decreased at the region rostral to the injury in riluzole-treated rats compared to the vehicle group, indicating potentially reduced neuroinflammatory activity. MRI metrics correlated temporally with behavioral measures of injury severity and recovery. Histological analysis spatially validated MRI-revealed myelination and neuroinflammation status and confirmed differences between the drug and vehicle treatment groups. Quantitative MRI is well suited for monitoring and quantifying the efficacy of pharmacological treatments in preclinical spinal cord injury models. Multiparametric MRI changes in white matter myelination (qMT PSR) and neuroinflammation (CEST APT) in the injured spinal cord were related to

**Abbreviations:** APT, amide proton transfer; BBB, Basso, Beattie, and Bresnahan; CEST, chemical exchange saturation transfer; DAB, 3,3'-diaminobenzidine; GFAP, glial fibrillary acidic protein; H&E, hematoxylin and eosin; HBC, 2-hydroxypropyl- $\beta$ -cyclodextrin; Iba-1, ionized calcium-binding adaptor protein-1; LFB, Luxol Fast Blue; PSR, pool size ratio; qMT, quantitative magnetization transfer; SCI, spinal cord injury.

John C. Gore and Li Min Chen equally guide the study.

This is an open access article under the terms of the [Creative Commons Attribution-NonCommercial-NoDerivs](https://creativecommons.org/licenses/by-nc-nd/4.0/) License, which permits use and distribution in any medium, provided the original work is properly cited, the use is non-commercial and no modifications or adaptations are made.

© 2025 The Author(s). *NMR in Biomedicine* published by John Wiley & Sons Ltd.

injury severity, behavioral deficits, and recovery progression over time. Both imaging metrics captured enhanced recovery from the neuroprotective drug riluzole, supporting the practical utility of these MRI biomarkers.

## 1 | Introduction

Millions of people are affected by spinal cord injuries (SCI), which result in severe disruptions in motor, sensory, and autonomic function [1, 2]. Post-SCI, long-term chronic symptoms such as bladder dysfunction, motor function deficits, and pain sensitization severely compromise the quality of lives of patients with SCI throughout their lives after injury [3, 4]. Despite diagnostic advances and improved understanding of the molecular mechanisms driving SCI pathologies, few treatments exist that successfully target these pathological changes after SCI, a situation exacerbated by the lack of non-invasive tools for longitudinal monitoring of recovery processes. Here, we report the development and application of noninvasive multiparametric magnetic resonance imaging (MRI) for assessing spinal cord tissues after injury and demonstrate how they may be used to evaluate the efficacy of SCI treatments over time.

The pathological progression of SCI is critically influenced by post-injury neuroinflammatory processes, including activation of pro-inflammatory cytokines [5] and recruitment of inflammatory activation in cells such as astrocytes and microglia [6, 7]. The progressive neuroinflammatory activity can deter axonal regeneration and intensify injury severity through processes such as toxic free radicals [8] and glial scar formation [9], leading to long-term chronic SCI pathological symptoms, including progressive neuropathic pain [10] and diminished motor function recovery [11]. Neuroinflammation can also promote demyelination, another degenerative process that occurs post-SCI [12]. Initial myelin degradation is caused by the direct injury mechanism, leading to axonal tissue damage, typically due to blunt force trauma to the region [13]. Further white matter demyelination occurs as a result of the cascading post-injury degenerative processes, including the post-injury neuroinflammatory response [14], Wallerian degeneration [15], and glutamate excitotoxicity [16]. Demyelination of spinal cord tracts post-injury leads to further disruption of spinal cord signaling conduction, thereby exacerbating post-injury sensory-motor deficits [17]. Potential SCI treatments commonly target post-SCI neuroinflammation and promote remyelination in the damaged spinal cord axons [18]. Thus, monitoring neuroinflammation and myelination post-SCI non-invasively is crucial for characterizing injury severity, monitoring injury progression, and assessing responsiveness to treatments.

MRI is capable of acquiring quantitative images generated using several different contrast mechanisms, allowing us to non-invasively and comprehensively evaluate structural and molecular changes within the spinal cord following injury over time. Chemical exchange saturation transfer (CEST) imaging is an MRI method that is capable of monitoring concentration changes of some molecules of interest [19], including several essential metabolites and neurotransmitters affected by neuroinflammation such as glutamate [20, 21]. We have previously demonstrated its use in rats subjected to lumbar contusion SCI [22]. Quantitative MRI methods can also indirectly assess myelin concentrations in both the brain and spinal cord [23]. In particular, quantitative

magnetization transfer imaging (qMT) has the acquisition speed and high spatial resolution necessary for in vivo imaging of myelin content [24]. In previous rat and squirrel monkey SCI studies, we have shown that qMT is capable of tracking demyelination post-injury, and the results were validated using gold standard post-mortem histological staining for myelin content [25–27].

Multiparametric MR imaging of pathophysiological changes after SCI is well suited for obtaining a basic understanding of recovery processes but sequential MRI acquisitions may also be valuable for determining the optimal time window, targets, and effectiveness of therapeutic interventions. We postulate that qMT and CEST imaging biomarkers can be used to assess traumatic injury-induced neuroinflammation and demyelination and to report the effects of interventions over time. To demonstrate this capability, we studied the effects of riluzole, an anti-glutamatergic neuroprotective drug that has been FDA-approved for use for treating a wide range of neurodegenerative disorders and which is currently being studied in preclinical and clinical trials as a neuroprotective treatment for SCI [28, 29]. Previous preclinical experiments have demonstrated that administration of riluzole post-injury results in improved spinal cord structural integrity and increased motor function recovery in treated rats [30]. Thus, the neuroprotective treatment is well suitable for use to evaluate potential noninvasive SCI imaging biomarkers. We herein demonstrate the use of CEST and qMT imaging metrics as noninvasive biomarkers for neuroinflammation and demyelination of injured spinal cord, validate their sensitivity and specificity for detecting effects of riluzole treatment, and relate the changes in MRI metrics to sensorimotor and pain behaviors. Our results demonstrate the sensitivity, specificity, and behavioral relevance of MRI CEST and qMT metrics to underlying spinal cord pathology of neuroinflammation and demyelination. We confirm that riluzole as a neuroprotective drug showed therapeutic efficacy in reducing SCI-associated neuroinflammation and neurodegeneration.

## 2 | Materials and Methods

### 2.1 | Animal Preparation

Sixteen adult male Sprague–Dawley rats weighing approximately 275–300 g were studied. Each animal was initially sedated with 2%–3% isoflurane and then kept free breathing while under anesthesia using isoflurane (0.5%–1.5%) delivered by 70/30 N<sub>2</sub>O/O<sub>2</sub> gas mixture during the MRI sessions. Respiration rates were maintained between 30 and 60 breaths/min by adjusting isoflurane concentrations. Vitals signs, including respiration pattern and rectal body temperature, were monitored and recorded throughout each imaging session. For MRI scans, animals were placed in a supine position on a customized bed. A customized 2 × 2 cm quadrature surface coil [31], designed specifically for rat spine imaging, was placed under the back of the rat for scanning. The bed has built-in side and top plates that can be used to restrain body movement by securing the plates on the abdomen. All the procedures were performed according to

NIH animal research guidelines and were approved by our local Institutional Animal Care and Use Committee.

## 2.2 | SCI

All rats underwent contusion injury under surgical-level anesthesia. A 5–6 cm incision was followed by a laminectomy on the dorsal side of the spine to expose the T12–L1 spinal cord segments. An Infinite Horizon impactor (Precision Systems and Instrumentation) was used to create a midline moderate contusion injury at the lumbar L1 level. The injury was created using a 2-mm-diameter probe, applying a constant force of 160 kDynes with a 1-s dwell time. Post-operative care included administration of analgesics (5–15 mg/kg carprofen), antibiotics (15–20 mg/kg enrofloxacin), and manual expression of the bladder when necessary.

## 2.3 | Riluzole and 2-Hydroxypropyl- $\beta$ -Cyclodextrin (HBC) Vehicle Treatments

Rats with SCI were divided into two groups: treatment and vehicle control. Riluzole was prepared following the methods described in Wu et al. [30]. Riluzole powder (Sigma-Aldrich, VWR) was dissolved in 30% w/v of 2-hydroxypropyl- $\beta$ -cyclodextrin (HBC, MilliporeSigma) to create a final stock of 8 mg/mL concentration. The final product was filtered through a 0.22- $\mu$ m syringe filter for sterilization. The rats in the riluzole treatment group ( $N=8$  rats) received 4 mg/kg of riluzole every 12 h through intraperitoneal (IP) injections for 2 weeks. The rats in the HBC vehicle group ( $N=8$  rats) received 30% w/v HBC every 12 h through IP injections in the same schedule as the treatment.

## 2.4 | Imaging Schedule

Riluzole treatment and HBC vehicle rats underwent MRI scans at multiple time points after surgery, at 3–4 days (Week 1), Week 2, Week 4, and Week 8 post-injury. Not every rat received MRI scans at every time point, as some rats dropped out of the study due to complications from the injury. The total number of rats included in the final analysis is reported in the figure legends.

## 2.5 | In Vivo MRI Data Acquisition

MR imaging studies were performed on a Magnex horizontal 9.4-T magnet with a Bruker (Billerica, MA) console using

sequence that incorporates a Gaussian RF offset pulse at 5000 Hz and 820° flip angle (TR/TE = 200/3 ms; FOV = 32 × 32 mm<sup>2</sup>; matrix size = 128 × 128, slice thickness = 3 mm [axial], 0.50 mm [coronal] and 0.75 mm [sagittal], flip angle = 35°), serving as a reference for slice selection in subsequent qMT and CEST scans to capture the dorsal column at the site of the injury and for coregistration of quantitative images acquired at different sessions. The MTC images were also used to determine the lumber enlargement and the level of spinal cord segments.

The qMT axial orientation images were acquired using a modified FLASH sequence with Gaussian saturation pulses at two saturation powers (flip angle = 820°, 220°), and 8 logarithmically scaled RF offsets from 1000 to 80,000 Hz, and an additional at 6000 Hz (TR/TE = 28/2.97 ms, NEX = 8, FOV = 32 × 32 mm<sup>2</sup>; matrix size = 128 × 128; slice thickness = 3 mm [axial]).

CEST imaging data were collected using a continuous wave CEST sequence with a 2.0-s rectangular irradiation pulse at 1  $\mu$ T power, followed by a multishot spin-echo echo-planar imaging sequence (two shots; TR/TE = 3000/29.59 ms; FOV = 32 × 32 mm<sup>2</sup>; matrix size = 96 × 96, slice thickness = 3 mm [axial], 0.8 mm [coronal]). The 33 RF offset frequency points were chosen to densely sample around specific pools of interest between –5.0 and 5.0 ppm (–2000 to 2000 Hz). Two 3-mm thickness axial slices were chosen, one rostral and caudal to the injury site, along with one 0.8 mm thickness coronal orientation slice to generate CEST pool amplitude maps for each molecular pool of interest.

MRI parametric maps were also collected during each scan acquisition for potential artifact corrections. T<sub>1</sub> maps were acquired using an inversion recovery sequence. T<sub>2</sub> maps were acquired using a multislice multiecho (MSME) sequence. B<sub>0</sub> maps are acquired using a multigradient echo sequence. B<sub>1</sub> maps were acquired using the double-angle method. Scan parameters are provided in the supplementary materials.

## 2.6 | MRI Image Analysis and Quantification

### 2.6.1 | qMT

We used the Henkelman–Ramani two-pool model for qMT data fitting [32], as previously optimized for rat spinal cord imaging [25]. The MT-weighted MR signals collected at multiple offset resonance frequencies ( $\Delta f$ ) were expressed as a function of irradiation amplitudes of continuous wave power equivalent ( $\omega_{CWPE}$ ), proportional to the square of the saturation pulse flip angles ( $\theta_{sat}$ ), using the following signal equation model:

$$S(\omega_{CWPE}, \Delta f) = \frac{M_0 \left( R_{1b} \left[ \frac{RM_{0b}}{R_{1a}} \right] + R_{RFB}(\omega_{1CWPE}, \Delta f, T_{2b}) + R_{1b} + \frac{RM_{0b}}{F} \right)}{\left[ \frac{RM_{0b}}{R_{1a}} \right] \left( R_{1b} + R_{RFB}(\omega_{1CWPE}, \Delta f, T_{2b}) \right) + \left( 1 + \left[ \frac{\omega_{CWPE}}{2\pi\Delta f} \right]^2 \left[ \frac{1}{T_{2a}R_{1a}} \right] \right) \left( R_{RFB}(\omega_{1CWPE}, \Delta f, T_{2b}) + R_{1b} + \frac{RM_{0b}}{F} \right)}$$

a 2 × 2 cm<sup>2</sup> rectangular transmit-receive quadrature radiofrequency (RF) coil [31]. High-resolution structural magnetization transfer contrast (MTC) MRI images in all 3 spatial planes (axial, coronal, and sagittal) were acquired with a gradient echo

where  $a$  and  $b$  are the free water and macromolecular water pools, respectively.  $F$  is the pool size ratio (PSR), or the ratio of the macromolecular water and free water pools ( $M_{0b}/M_{0a}$ ). In previous literature, PSR correlates strongly with myelin content in spinal cord white matter tracts [33].  $M_{0a}$  and  $M_{0b}$  are the fully

relaxed magnetization signals in the free water and macromolecular water pools.  $M_0$  is the magnetization signal without MT contrast,  $R_{\text{RFB}}$  is the macromolecular pool rate of saturation;  $R_{1a}$  and  $R_{1b}$  are the longitudinal relaxation rates for the free water and macromolecular water pools. For our model,  $R_{1b}$  is set constant at  $1 \text{ s}^{-1}$ , whereas  $R_{1a}$  is dependent on the observed longitudinal relaxation rate  $R_{1\text{obs}}$ , described in the model as

$$R_{1a} = R_{1\text{obs}} - \frac{RM_{0b}(R_{1b} - R_{1\text{obs}})}{R_{1b} - R_{1\text{obs}} + \frac{RM_{0b}}{F}}$$

Combining both equations, the acquired qMT signal is fitted using the Ramani–Henkelman model in order to calculate  $F$ ,  $M_0$ ,  $RM_{0b}$ ,  $T_{2a}$ , and  $T_{2b}$ . Model fitting was performed using MATLAB 2021B (MathWorks, Natick, MA) using a least-squares fitting algorithm minimizing the squared two-norm of the residuals. Voxel-by-voxel model fitting was used to generate PSR maps from the acquired axial orientation images. Average white matter PSR values were calculated using ROI-based segmentation, where fitted voxels with residual greater than 0.01 and voxels with PSR values greater than 0.2 were excluded from statistical analysis.

## 2.6.2 | CEST

CEST MRI data analyses were performed using MATLAB 2020B. CEST images were used to generate Z-spectra from selected gray matter regions of interest (ROIs) in both axial slices of the spinal cord, by first normalizing the image signals  $S$  to a reference scan  $S_0$  collected at an offset frequency of 100,000 Hz:

$$Z = \frac{S}{S_0}$$

Z-spectra were fit to a series of 5 Lorentzian peaks:

$$\text{Signal}(\Delta) = 1 - \sum_{i=1}^n A_i \left[ 1 + \left( \frac{\Delta - \Delta_{oi}}{0.5 * W_i} \right)^2 \right]^{-1}$$

which are each defined by peak amplitude  $A$ , frequency offset  $\Delta_o$ , and width  $W$ . The 5 Lorentzian peaks were centered at  $-3.5$  ppm (nuclear Overhauser effect [NOE]),  $-1.6$  ppm (NOE), 0 ppm (water), 2 ppm (amine), and 3.5 ppm (amide proton transfer [APT]), the same model implemented in our previous rat SCI studies [22]. Peak fittings were performed in MATLAB using a nonlinear optimization algorithm [34]. Amplitudes for each of the 5 fitted Lorentzian peaks were averaged across subjects for the riluzole treatment and HBC vehicle groups at each time point. Coronal orientation spatial maps of each molecular pool were generated using voxel-by-voxel fitting to the 5 Lorentzian pool model. Statistical comparisons of CEST/NOE peak amplitudes between riluzole treatment and HBC vehicle groups were performed using a nonparametric Wilcoxon rank-sum test corrected for false discovery rate.

## 2.7 | Behavioral Data Acquisition and Analyses

Hindlimb locomotor and somatosensory deficits after SCI were quantified using a battery of behavioral tests. Baseline

measurements were collected pre-SCI, followed by data collection on Day 1 post-injury and on a weekly basis from Week 1 until Week 8 post-injury. Basso, Beattie, and Bresnahan (BBB) Locomotor Rating scores [35] and open field [36] tests were used to measure locomotor functionality and coordination deficits for each limb post-SCI. Somatosensory functions, including tactile, thermal, and nociceptive responses, mechanical allodynia, and thermal hyperalgesia, were evaluated using Von Frey filament tests [37] and hot plate latency measurements [38].

Open field tests measured locomotor activity of the animal subjects in an empty plexiglass open field chamber using a system of infrared beams. Movement in the chamber resulted in beam breaks, which were recorded as a measured movement activity value. Each rat was habituated in the open field chamber for at least one 30-min session. Baseline BBB scores were also collected for each hindlimb during the open field sessions.

For manual Von Frey filament tests, the animals were placed in a small plexiglass chamber, with a mesh grid floor underneath. Monofilaments of specific force values were applied perpendicular to the hindpaw, and each filament was applied 10 times consecutively for 1 s durations (2, 4, 6, 8, 10, 15, 26, and 60 g). A positive response was recorded if the rat demonstrated at least 5 out of 10 responses at a specific filament strength, including paw withdrawal or any other physical stimulus response such as licking or shaking their paw after the filament was applied.

The hot plate test was performed by placing the rats on a hot plate set at  $55^\circ\text{C}$ , and the time to elicit a withdrawal or pain response was measured, with a 15-s time limit. The hot plate test was not performed during the initial 2 days post-injury, due to the administration of post-operative analgesics. Statistical comparison between the treatment and vehicle groups at different time points was performed using a non-parametric Wilcoxon rank-sum test corrected for false discovery rate.

Behavioral measurements in the treatment and vehicle groups at different time points were compared and evaluated using a nonparametric Wilcoxon rank-sum test with false discovery rate correction. Temporal correlations between behavioral measurements and qMT PSR and CEST pool amplitude measurements were calculated using Pearson's correlation coefficients.

## 2.8 | Postmortem Histological Analysis

Animals ( $N=2$  treatment rats  $\times$  2 sections per stain,  $N=2$  vehicle rats  $\times$  2 sections per stain) were euthanized 8 weeks post-injury, and spinal cord tissues were perfused, fixed with 10% formalin, paraffin-embedded, transversally sectioned, and processed in our Translational Pathology Shared Resource Core. Histological staining included blue hematoxylin for nuclei, brown 3,3'-diaminobenzidine (DAB) for selected biomarkers of interest (antibodies for inflammatory cells), and hematoxylin and eosin (H&E) for general tissue microstructure. Immunostaining included ionized calcium-binding adaptor protein-1 (iba-1) for

activated microglia [39], glial fibrillary acidic protein (GFAP) for astrocytes [40], and Luxol Fast Blue (LFB) for myelin density [41].

Images of histological sections (slides) of the stained spinal cord tissues were captured at the Digital Histology Shared Resource Core at VUMC using a high throughput Leica SCN400 Slide Scanner automated digital image system from Leica Microsystems. Whole slides were imaged at 20× magnification to a resolution of 0.5 μm/pixel. We used the open-source histological analysis software QuPath [42] to quantify both iba-1-positive activated microglia cells and GFAP-positive astrocytes by identifying the brown DAB “positive cells” from the blue hematoxylin “DAB-negative cells.” Histological quantification was performed by selecting 2 spinal cord sections from each subject and segmenting the sections as rostral and caudal to the spinal cord injury site using 2 separate rectangular ROIs to define each segment. QuPath analysis tools were used to first classify and separate stain vectors between DAB and hematoxylin stains and then segment spinal cord tissue from background. Next, the automated cell detection program counted all hematoxylin-stained cells. Finally, positive DAB-stained cells were classified using histogram-based thresholds based on DAB cell nucleus mean pixel-intensity values. The percentage of positive cells identified for each section, rostral and caudal to the spinal cord injury site, were averaged across all cohort datasets and compared between riluzole treatment and HBC vehicle sections using an unpaired-*t* test (two-way, alpha=0.05). For analysis of the LFB-stained spinal cord tissue sections, QuPath analysis tools

were used to quantify the LFB stain intensity in a defined ROI, measuring myelin content in the selected area. Stain intensities were compared between treatment and vehicle groups using an unpaired-*t* test.

### 3 | Results

#### 3.1 | qMT Captured Loss of Myelination After SCI and Improved Recovery in Riluzole-Treated Rats

qMRI-derived PSR measurements reflect the myelination status of the white matter tissue. Healthy and intact white matter axons exhibit higher PSR values. Transverse axial spinal cord PSR maps from the riluzole treatment group indicated significantly higher PSR values in white matter voxels at the epicenter of injury (Figure 1A; mean ± SD: PSR=0.106 ± 0.029), compared to white matter PSR values in PSR maps from the HBC vehicle treatment group (Figure 1B; 0.0698 ± 0.020, *p*=0.0426), at Week 1, Week 2, and Week 4 post-injury. The treatment group white matter PSR values are comparable to our previous studies acquired from normal rat lumbar spine white matter regions (PSR=0.1247) [25]. Similarly, the early injury time point PSR values from the vehicle group are almost identical to the PSR values in untreated SCI rats from our previous studies (PSR=0.0710) [25].

Next, we quantified PSR values at three segmental locations using MTC contrast-weighted anatomical images as the guide

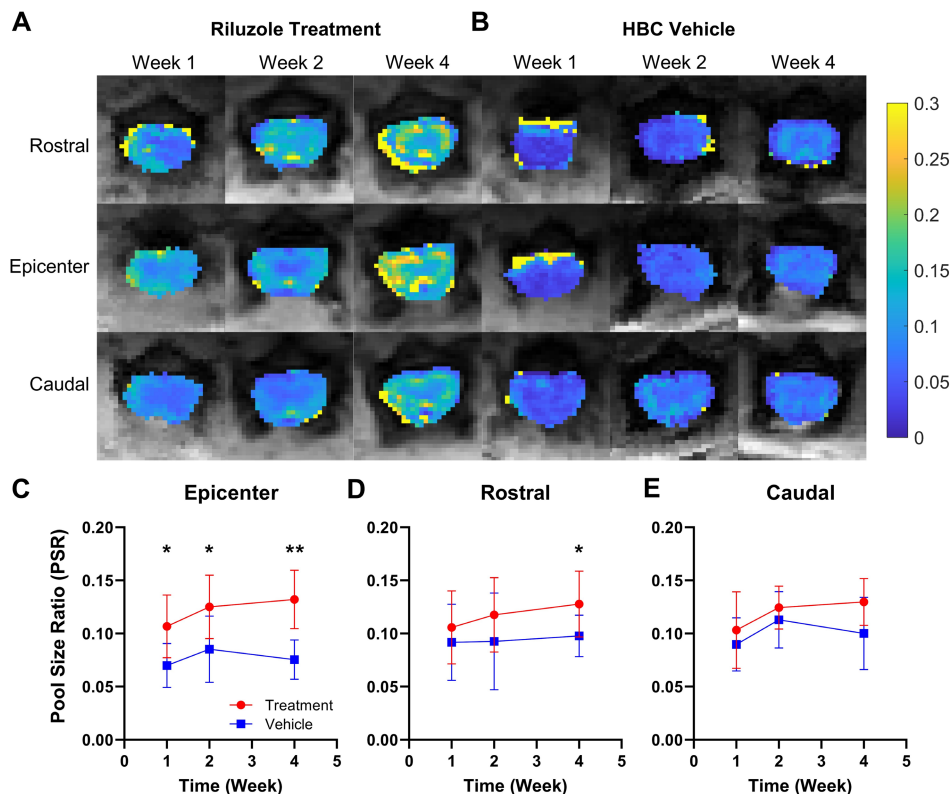


**FIGURE 1** | Comparison of qMT PSR maps and values along the spinal cord in riluzole-treated versus HBC vehicle-treated SCI rats. (A,B) Representative PSR maps acquired from injury epicenter, rostral, and caudal to the injury at Week 1 and Week 2 to Week 4 post-injury in rats that received riluzole (A) versus HBC vehicle (B) treatment. (C–E) Average white matter PSR values comparison between treatment and vehicle groups, at (C) injury epicenter, (D) rostral, and (E) caudal, from Week 1 to Week 4. \**p* < 0.05, \*\**p* < 0.005, non-parametric Wilcoxon rank-sum test.

for selecting white matter ROIs, as white matter–gray matter contrast was not evident in all PSR maps. At the injury epicenter, the PSR values of the white matter ROI showed significant higher and progressive increases during the 4-week post-injury period in the riluzole treated (Figure 1C; Week 2 =  $0.125 \pm 0.029$ , Week 4 =  $0.132 \pm 0.027$ ) versus the HBC vehicle-treated SCI rats (Week 2 =  $0.0852 \pm 0.031$  and  $p = 0.0401$ , Week 4 =  $0.0754 \pm 0.018$  and  $p = 0.0012$ ), suggesting enhanced remyelination in the riluzole-treated SCI rats over time. Rostral to the injury center ROI, the white matter PSR values of the treatment group ( $0.131 \pm 0.030$ ) were significantly higher than vehicle treatment group ( $0.0968 \pm 0.019$ ,  $p = 0.0289$ ) during the later weeks of the injury progression. At the caudal ROI location, no significant differences in PSR values were observed between the rats in the two groups. This suggests that riluzole enhances the remyelination process of spinal cord white matter tracts post-injury.

### 3.2 | CEST Detected APT Pool Amplitude Increases Following SCI and Subsequent Decreases With Riluzole Treatment

CEST Z-spectra were acquired from two different imaging orientations: axial (transverse) and coronal (along the cord) over 8 weeks. At Week 1 post-injury, Z-spectra and fitting (Figure 2A,B) derived from ROIs on axial orientation CEST images showed that the 3.5 ppm APT pool amplitude decreased significantly in the riluzole treatment group compared to the vehicle control group. Peak values extracted from the rostral spinal segments to the injury epicenter showed no significant difference at  $-3.5$ ,  $-1.6$ , and  $2$  ppm. However, the 3.5 ppm peak amplitude in the treatment group (mean  $\pm$  SD:  $0.0244 \pm 0.0127$ ) was significantly lower than the vehicle group ( $0.0669 \pm 0.0483$ ,  $p = 0.0378$ ) (Figure 2C). No significant differences between groups were found during the later weeks post-injury.

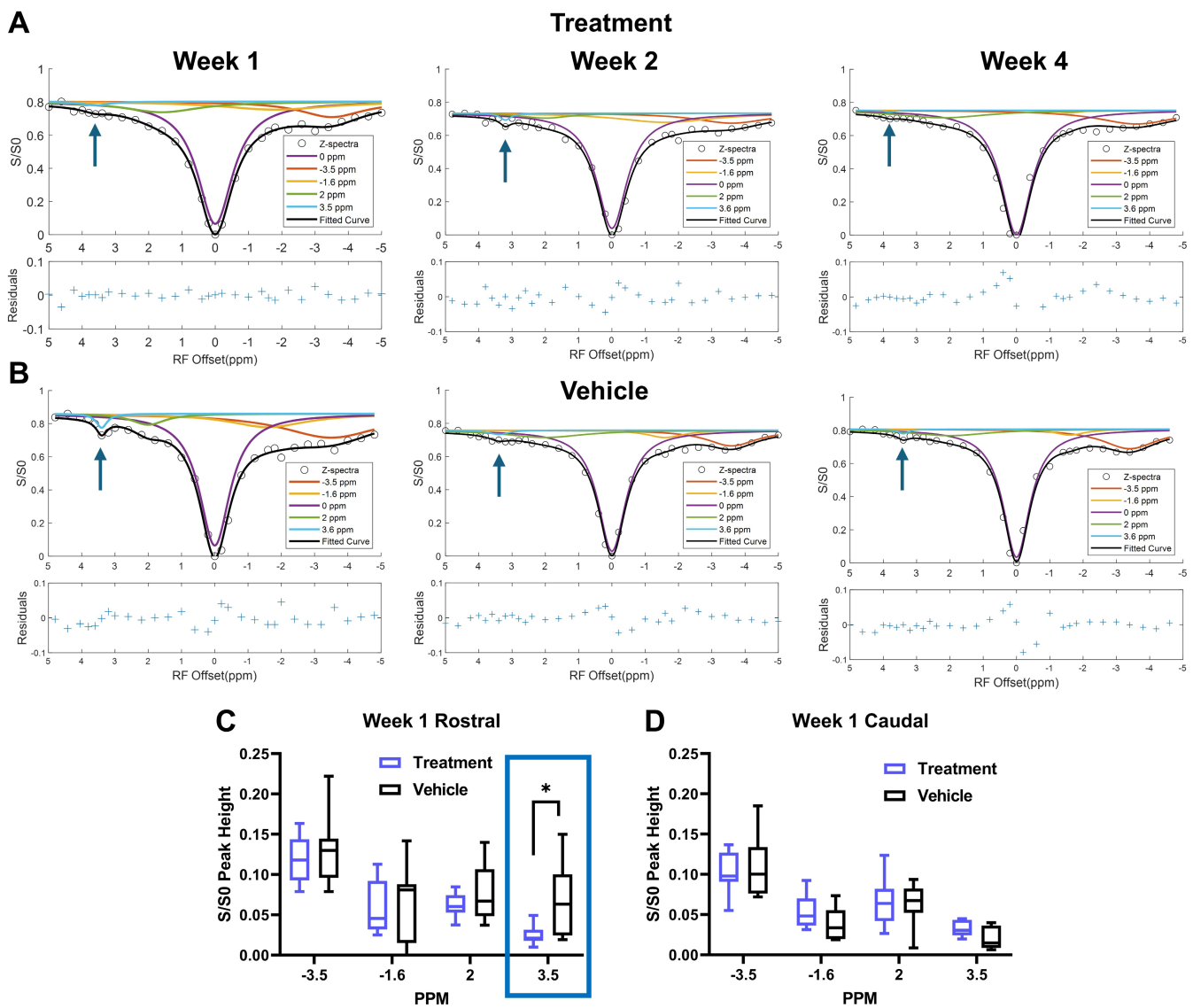


**FIGURE 2** | Comparison of CEST axial Z-spectra data between riluzole treatment and HBC Vehicle controls. (A,B) Z-spectra with model fitting Lorentzian curves for riluzole treatment and vehicle rats from Weeks 1 to 4, rostral to the injury site. Blue arrow indicates CEST APT (3.5 ppm) molecular pool. (C,D) Box plots of peak amplitudes for each Z-spectra pool from rostral and caudal slices, comparing riluzole and vehicle rats during Week 1 post-injury. \* $p < 0.05$ , non-parametric Wilcoxon rank-sum test.

Spatial maps of molecular pools derived from coronal orientation CEST images at Week 1 post-injury (Figure 3A,C) revealed similar changes in the 3.5 ppm APT pool, as indicated by the high pool amplitude yellow voxels present at the epicenter in the representative APT pool map from the HBC vehicle group, which are not visible in the representative riluzole treatment APT pool map. The spatial line profiles of the APT pool amplitudes plotted along the long axis of the cord showed increases at the epicenter of injury in the HBC vehicle group (Figure 3D,F), but the increase is absent in the riluzole treatment group (Figure 3B,E).

### 3.3 | Behavioral Testing Identified Improved Functional Recovery After Administration of Riluzole

All four behavioral tests detected recovery differences between the riluzole-treated and vehicle-treated rats with SCI (Figure 4). The riluzole treatment group showed significantly improved motor function recovery, as indicated by higher BBB scores and normalized open field activity (Figure 4A,B), during the first 2 weeks after injury. During later weeks post-injury (Weeks 4–8 post-injury), the averaged BBB scores of riluzole-treated rats were also significantly higher than vehicle treatment rats (mean  $\pm$  SD:  $13.00 \pm 4.99$  for treatment and  $8.75 \pm 4.37$  for vehicle at Week 4 post-injury,  $p=0.0370$ ). Open field activity measures showed no significant differences between the two groups

post-injury. The treatment group also showed longer response times (Week 2 =  $3.40 \pm 0.56$  s, Week 4 =  $3.12 \pm 0.61$  s) on the hot plate test compared to the vehicle group (Week 2 =  $3.11 \pm 0.64$  s, Week 4 =  $2.68 \pm 0.75$  s), indicating that the treatment group exhibits reduced heat pain sensitization at the later weeks post-injury.

### 3.4 | Temporal Correlations Between qMT and CEST Metrics with Behavior During Recovery

Spatially coincident qMT PSR and CEST APT metrics were correlated temporally with behavioral measurement changes (Figure 5A,B) for riluzole and HBC vehicle treatment groups. Only the PSR value at the injury epicenter and 3.5 ppm CEST values at the rostral ROI showed significant differences between the two treatment groups, so we correlated these two, along with the measures derived from all defined regions (combined), with four behavioral time courses. Both PSR and APT pool amplitude measures acquired from the epicenter of injury and rostral to the injury (Tables 1 and 2) showed significant correlations with the BBB score (treatment PSR – BBB score  $r=0.956$  and  $p=0.0436$ ) and hot plate test (treatment PSR – HP time  $r=-0.952$  and  $p=0.0436$ , treatment APT – HP time  $r=-0.997$  and  $p=0.002$ ). PSR values and APT pool amplitudes were combined between all defined regions for the treatment (qMT combined – BBB score  $r=0.960$  and  $p=0.0399$ , qMT combined – HP time  $r=-0.968$  and  $p=0.0317$ , APT combined – Von Frey  $r=-0.984$

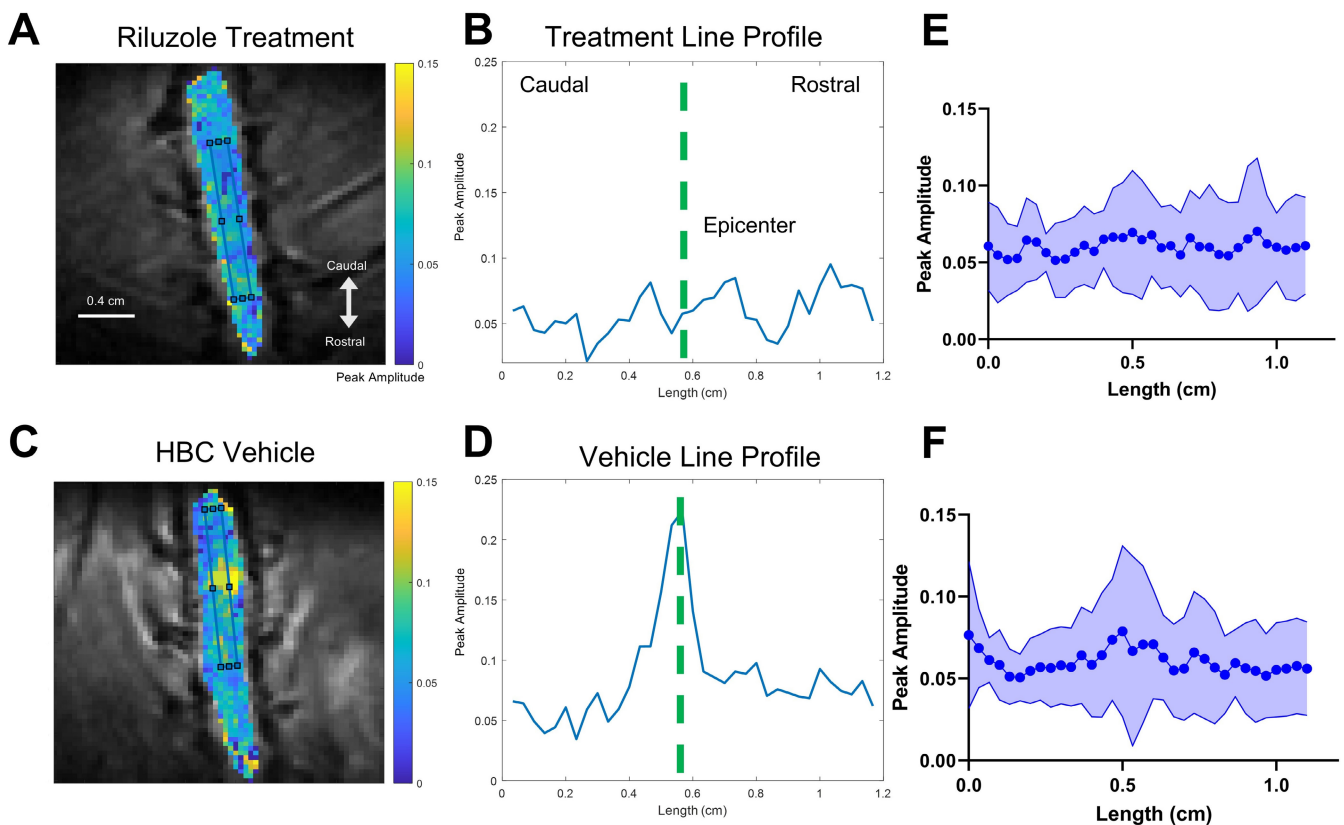


**FIGURE 3** | CEST coronal maps and spatial profile for the CEST 3.5 ppm pool at Week 1 post-injury. (A,B) Representative CEST (3.5 ppm) APT coronal map acquired from riluzole-treated rat, superimposed onto CEST image (A), with corresponding line profile showing decreased pool amplitude at and rostral to the epicenter (B). (C,D) HBC vehicle rat CEST (3.5 ppm) APT coronal map, superimposed onto CEST image, with corresponding line profile showing increased pool amplitude at the epicenter. (E,F) Group-level CEST 3.5 ppm line profiles, averaged across riluzole ( $N=8$ ) and vehicle ( $N=8$ ) treatment groups, with standard error of the mean shaded blue.

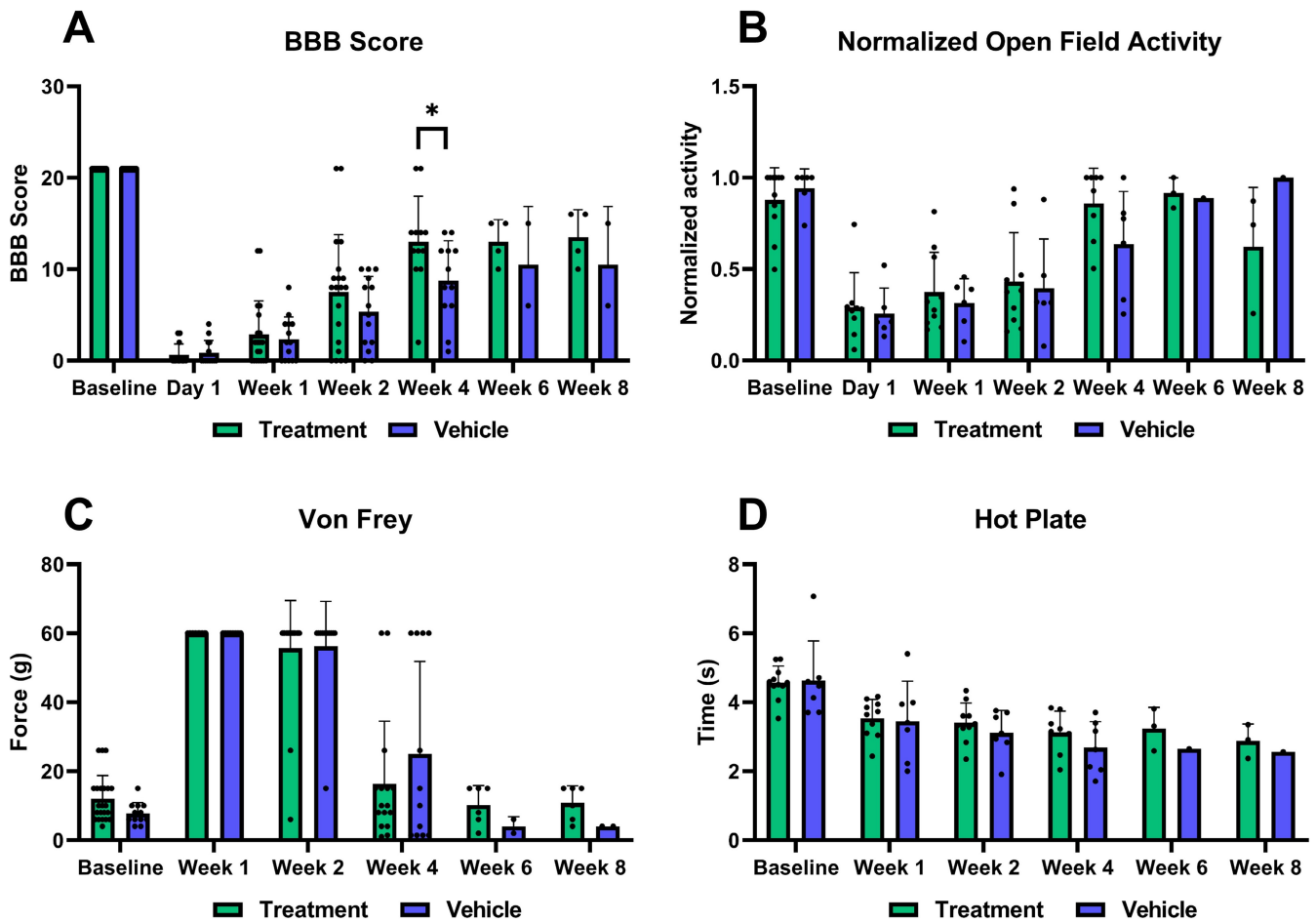


**FIGURE 4** | Comparison of hindlimb sensorimotor behaviors in SCI rats receiving riluzole versus HBC vehicle treatment. (A) Combined BBB scores for left and right hindlimbs. (B) Open field activity normalized to the highest measured activity session. (C) Combined Von Frey filament test thresholds for left and right hindlimbs combined. (D) Hot plate test reaction time measurements. \* $p < 0.05$ , non-parametric Wilcoxon rank-sum test.

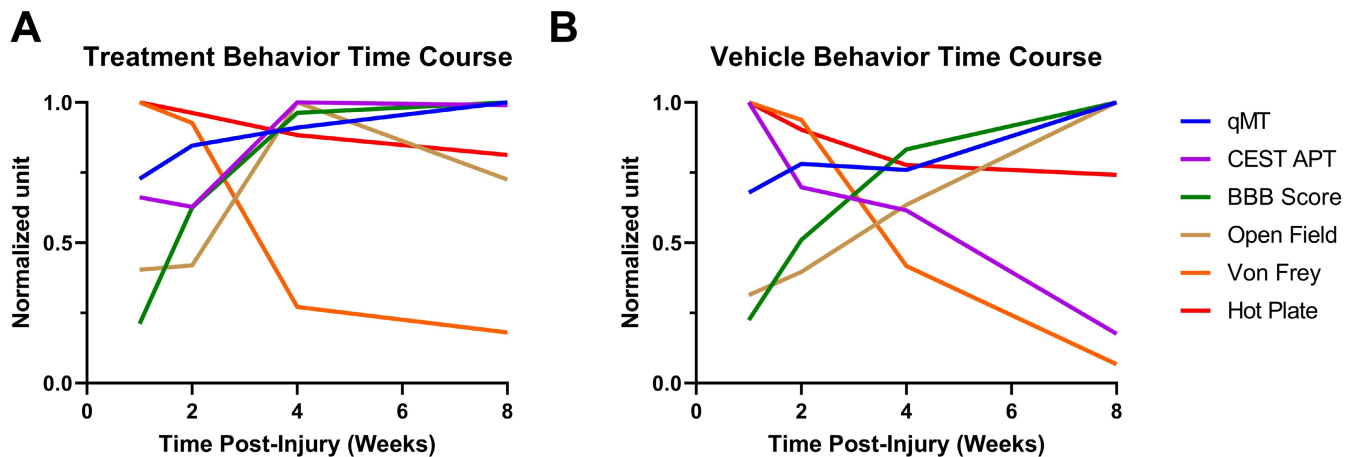


**FIGURE 5** | Temporal correlation of qMT and CEST imaging metrics to behavioral measurements of functional recovery. (A) Time course comparison between qMT PSR combined for all spatial regions and CEST APT combined compared to behavioral measurements for riluzole treatment group. (B) Time course comparison for HBC vehicle group.

and  $p = 0.0153$ ) and vehicle groups (CEST combined – open field  $r = -0.962$  and  $p = 0.0379$ ) and the combined metric also indicated significant correlation with all four behavioral tasks. To quantify whether PSR and APT differences between treatment and vehicle animals were correlated with corresponding behavioral differences between the two groups, the differential

values between treatment and vehicle were calculated for imaging and behavior measurements and temporally correlated (Table 3). Whereas no significant correlation values were found, strong correlations (greater than 0.7) were identified (epicenter PSR – open field  $r = 0.791$ ; epicenter PSR – Von Frey  $r = -0.924$ ; combined PSR – BBB score  $r = 0.724$ ; combined PSR – hot plate

**TABLE 1** | Treatment qMT/CEST: behavior correlation.

	qMT epicenter	CEST rostral	qMT combined	CEST combined
BBB score	0.956*	0.919	0.96*	0.851
Open field	0.632	0.683	0.663	0.922
Von Frey	-0.875	-0.941	-0.900	-0.984*
Hot plate	-0.952*	-0.997*	-0.968*	-0.899

Note: Treatment qMT/CEST MRI metrics temporal correlation with corresponding behavioral metrics. Red =  $|r| > 0.7$ . Values highlighted in red are strong correlations. \* $p < 0.05$ .

**TABLE 2** | Vehicle qMT/CEST: behavior correlation.

	qMT epicenter	CEST rostral	qMT combined	CEST combined
BBB score	0.73	-0.932	0.823	-0.934
Open field	0.852	-0.894	0.925	-0.962*
Von Frey	-0.744	0.852	-0.842	0.917
Hot plate	-0.676	0.907	-0.776	0.903

Note: Vehicle qMT/CEST MRI metrics temporal correlation with corresponding behavioral metrics. Red =  $|r| > 0.7$ . Values highlighted in red are strong correlations. \* $p < 0.05$ .

**TABLE 3** | Treatment-vehicle differential correlation.

	qMT epicenter	CEST rostral	qMT combined	CEST combined
BBB score	0.656	0.696	0.724	0.644
Open field	0.791	-0.597	0.754	-0.524
Von Frey	-0.924	0.354	-0.905	0.287
Hot plate	0.7	0.697	0.756	0.682

Note: Treatment-vehicle differential in qMT/CEST MRI metrics, temporal correlation with corresponding Treatment-vehicle differential in behavioral metrics. Red =  $|r| > 0.7$ , \* $p < 0.05$ . Values highlighted in red are strong correlations.

**TABLE 4** | qMT-CEST correlation.

Regions	Treatment	Vehicle
qMT-CEST rostral	0.957	-0.793
qMT-CEST caudal	0.568	-0.251
qMT-CEST combined	0.811	-0.970*

Note: Correlations between qMT and CEST MRI metrics for treatment and vehicle groups. Red =  $|r| > 0.7$ . Values highlighted in red are strong correlations. \* $p < 0.05$ .

$r = 0.756$ ). PSR values and APT pool amplitudes in spinal segments rostral to the injury region and combined regions were also strongly correlated for both treatment and vehicle groups (Table 4).

### 3.5 | Immunohistological Evaluation of Demyelination and Neuroinflammation

LFB staining for myelin revealed that spinal cord tissue sections from the riluzole treatment rats 8 weeks post-injury showed intact gray and white matter structural integrity (Figure 6A) and significantly increased stain intensity ( $0.8066 \pm 0.17$ ), compared to the

vehicle rat tissue sections (Figure 6B;  $0.4252 \pm 0.026$ ,  $p = 0.004$ ). The vehicle rat sections exhibited disrupted white matter structural integrity and tissue damage at the epicenter of injury.

Iba-1 (Figure 7A,B) and GFAP staining (Figure 7C,D) for activated microglia and astrocytes showed significantly increased percentage of Iba-1-positive cells (Figure 7E) from the HBC vehicle group spinal cord tissue sections (34.2%) compared to the treatment group (20.8%,  $p = 0.0074$ ), corresponding to increased activated microglia activity in the HBC vehicle group compared to the riluzole treatment group. No significant difference in GFAP-positive cells was found (Figure 7F), and no rostral-to-caudal differences were found for either inflammatory cell staining types in the treatment and vehicle groups.

## 4 | Discussion

### 4.1 | qMT PSR as an Imaging Biomarker of Post-Injury Demyelination and Treatment Efficacy

At the injury epicenter, qMT maps indicated significantly increased PSR values in white matter post-injury for the riluzole treatment group compared to the vehicle group, starting from

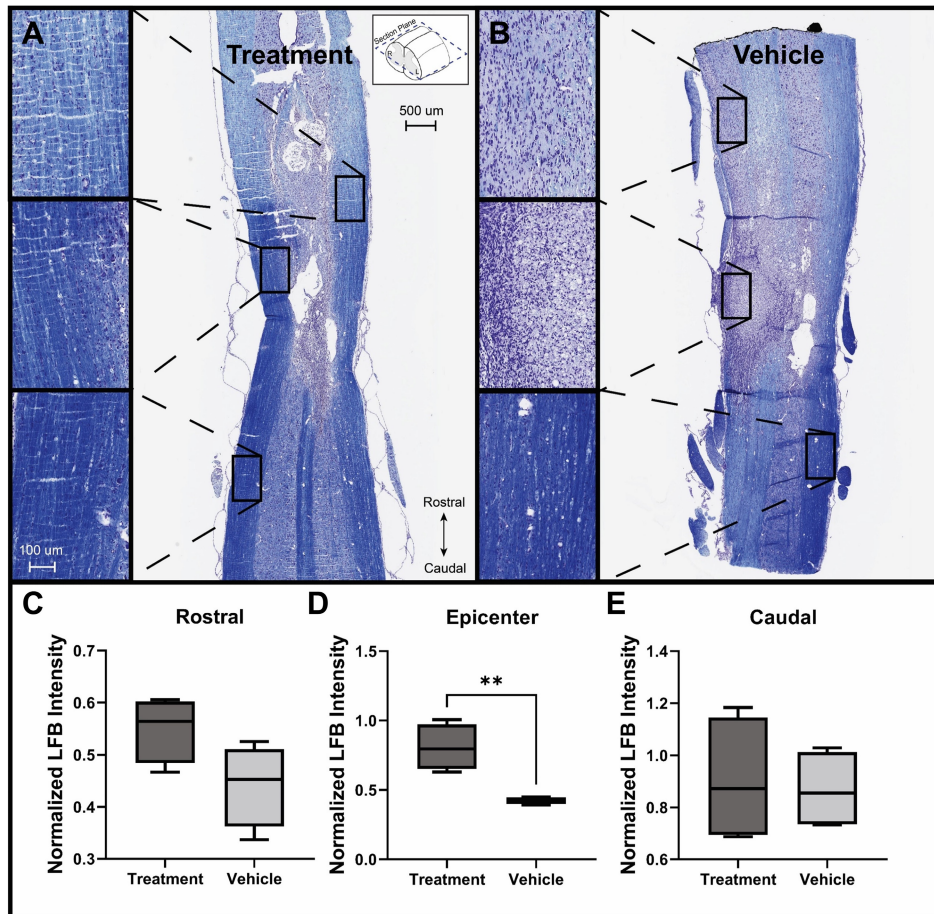


**FIGURE 6** | Luxol Fast Blue (LFB) validation of riluzole treatment reduction of demyelination. (A,B) Representative coronal sections of LFB-stained spinal cord tissue obtained from SCI rats that received riluzole (A) or vehicle (B) treatments, with zoomed-in representations of the tissue sections (at 20× magnification) at the center, rostral, and caudal to the injury epicenter. (C–E) Comparison of normalized mean LFB stain intensities at three ROIs: rostral (C), epicenter (D), and caudal (E) in SCI rats that received riluzole treatments ( $N=2$  rats  $\times$  2 sections) or vehicle ( $N=2$  rats  $\times$  2 sections). LFB intensity is significantly decreased in HBC vehicle group sections compared to riluzole treatment.  $**p < 0.005$ , non-parametric Wilcoxon rank-sum test.

Week 1 and extending into the later weeks post-injury. In the spinal cord, the immobile proton signal in white matter regions is mainly from water bound within the myelin layers covering the axons. Thus, PSR is an indirect measure of myelin concentration [33, 43–45] and may be used as a reporter of myelin status. The greater PSR values in rats who received riluzole treatment at the time of injury demonstrate that qMT PSR can be employed as a biomarker of neuroprotection against demyelination based on the effect of riluzole. PSR values for treatment rats progressively increased from Weeks 2 to 4, indicating that PSR may be a sensitive biomarker of enhanced remyelination in the treatment animals. The vehicle group showed little change in average PSR values over time in comparison. Segmental PSR values successfully differentiated between the treatment and vehicle and also revealed spatial differences in myelination changes post-injury. In the vehicle group, PSR values did not increase in the segment rostral to the injury site during the later weeks post-injury, whereas the treatment group showed gradual PSR increases in all three spatial segments of the spinal cord. The quantification of LFB stain of postmortem spinal cord tissue supports our interpretation of PSR values as indicating myelin content and myelination status.

#### 4.2 | CEST APT Pool Amplitudes as Biomarkers of Neuroinflammation and Response to Treatment

CEST Z-spectra from rostral to the spinal cord injury region identified a reduction in the APT pool in the riluzole treatment group at Week 1 post-injury, compared to the vehicle group. The APT molecular pool signal is typically related to proteins and small peptides [46], including metabolites associated with neuroinflammation. In other models of neurological disorders, such as traumatic brain injuries [47] and ischemic stroke [48], an increase in the APT pool amplitude correlated with elevated neuroinflammatory activity [49, 50]. This suggests that the reduction of the APT pool in the riluzole treatment group corresponds to reduced neuroinflammatory activity as a result of the neuroprotective treatment. This is further validated by the postmortem histological analysis, showing that the spinal cord sections from the riluzole treatment group exhibited significantly reduced activated microglia cell count compared to the HBC vehicle control group, signifying decreased neuroinflammation for the treatment group. Thus, changes in the APT pool amplitude may be used as a biomarker of neuroinflammation.

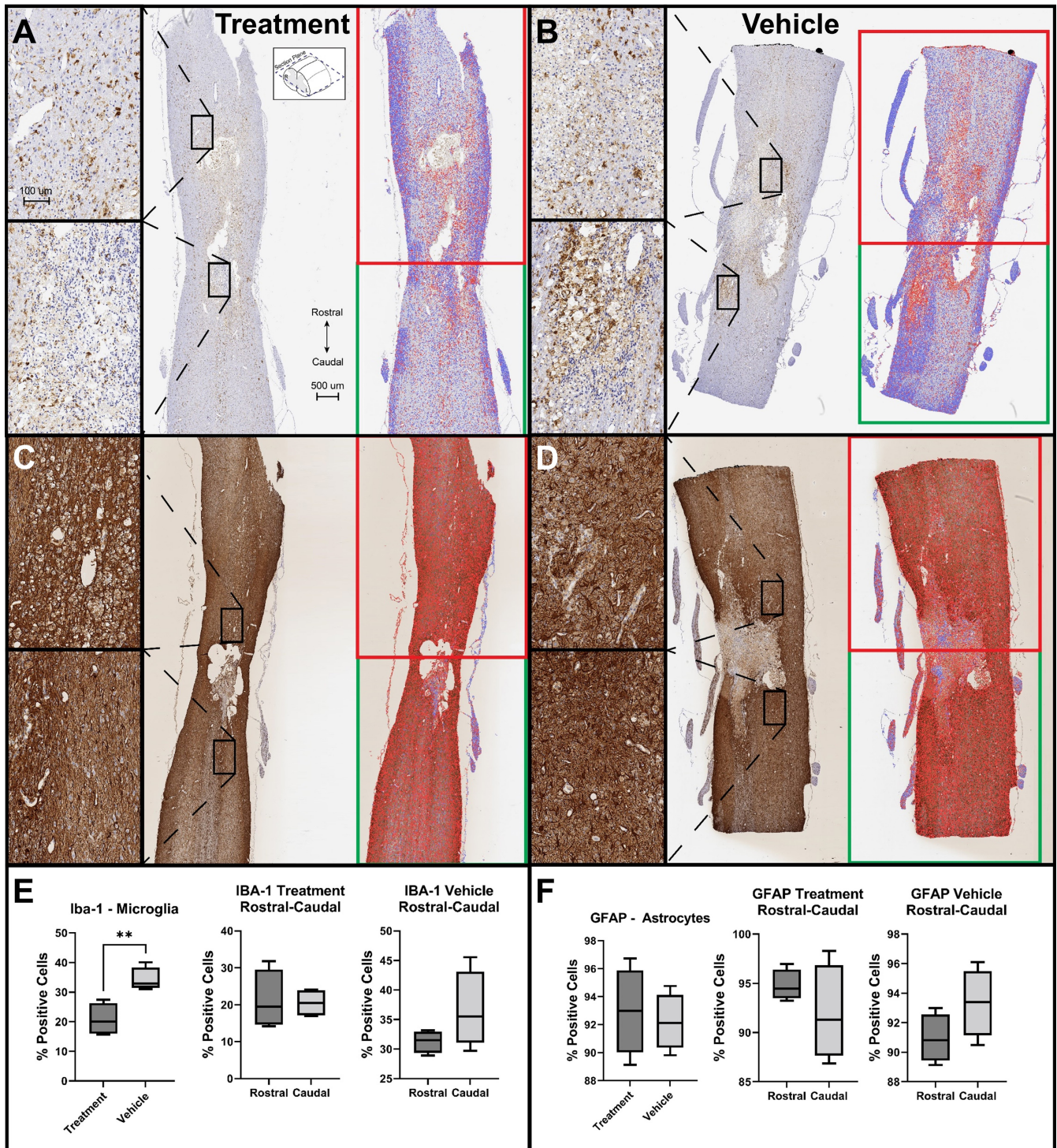


**FIGURE 7** | GFAP and Iba-1 validation of riluzole treatment reduction of neuroinflammation. Selected from serial coronal sections from lumbar spinal cord of a riluzole treatment rat and HBC vehicle rat 8 weeks after injury, sections stained for microglia marker iba-1 and astrocyte marker GFAP. All treatment ( $N=2$  sections  $\times$  2 rats) and vehicle sections ( $N=2$  sections  $\times$  2 rats) showed lasting injury with areas of reduced gray and white matter or deformation to tissue structure. (A) Iba-1-stained treatment section, with zoomed-in representations of the section at 20 $\times$  magnification rostral and caudal to the SCI region. Cell count analysis shows Iba-1-positive cells labeled in red, and negative cells labeled in blue. Rectangular ROIs dividing the section into rostral (red) and caudal (green) are shown. (B) Iba-1-stained vehicle spinal cord section, with cell labeling. (C) GFAP-stained treatment section at 20 $\times$  magnification rostral and caudal to the SCI region. (D) GFAP-stained vehicle section, with cell labeling. (E) There is a significant decrease in Iba-1-positive cell percent for treatment rats compared to vehicle. (F) No significant difference was observed in GFAP-positive cell percent for treatment compared to vehicle.  $**p < 0.005$ , non-parametric Wilcoxon rank-sum test.

### 4.3 | Behavioral Relevance of qMT PSR and CEST APT Imaging Metrics

The riluzole treatment group demonstrated improvements in motor function, particularly the BBB score, during the later weeks post-injury, compared to the vehicle group. They also exhibited decreased sensitivity to heat and pain stimulus in a hot plate test, indicating lack of hyperalgesia symptoms typically associated with SCI. This is consistent with previous preclinical riluzole treatment studies, where rats treated with riluzole also exhibited increased motor functionality with improved BBB scores compared to the vehicle group [30]. Functional recovery over time for both treatment and vehicle groups correlated temporally with both qMT PSR and CEST APT metrics, especially BBB score and hot plate response times. The results validate the functional relevance of both imaging biomarkers, as both show correspondence to behavioral recovery over time after the injury. These measures also show different correlations to each behavioral measure, which could be due to differences in the specific pathology to which each imaging parameter is sensitive. The qMT metric shows stronger correlation with motor function, whereas CEST APT is highly correlated with somatosensory function. For predicting recovery progression differences between the riluzole treatment and HBC vehicle groups, qMT appears to have greater sensitivity, shown by the stronger correlation values in the correlation analysis. Thus, using a multimodal imaging approach is appropriate for quantifying injury severity, recovery progression, and treatment efficacy, as different imaging biomarkers are more sensitive for monitoring different aspects of recovery. Our results indicate that administration of riluzole post-SCI successfully acts as a neuroprotective treatment that reduces post-injury neuroinflammation and demyelination and translates to corresponding motor and somatosensory behavior improvements in the treated rats.

### 4.4 | Histology Validated the qMT and CEST Metrics of Myelination Status and Neuroinflammation in Riluzole-Treated Rats

The myelin histological staining verified the distribution of myelin captured using qMT MRI, showing that qMT is capable of indirectly monitoring myelin changes in the spinal cord. Previous riluzole treatment preclinical studies used structural histology to demonstrate that riluzole preserves and reduces structural degradation in the spinal cord post-injury [30]. Although myelination was not explored in previous studies, our results are relatively similar, showing that the extent of post-injury demyelination is reduced in treatment rats, and the treatment group shows remyelination after injury, unlike the vehicle group.

### 4.5 | Clinical Relevance

We have successfully demonstrated that qMT PSR mapping can noninvasively probe myelination changes in spinal cord white matter tracts post-injury and the CEST APT molecular pool can identify concentration changes of metabolites related to neuroinflammatory activity.

Both metrics provide crucial information regarding the injury severity and recovery progression from SCI. The CEST APT and PSR parameters can differentiate between rats treated with riluzole, a neuroprotective drug that can improve motor and somatosensory function after SCI. Thus, we believe that quantitative MRI is highly suitable for quantifying the efficacy of different SCI pharmacological treatments in preclinical trials. CEST and qMT images may be acquired of human spinal cord [21, 24] and thus can be applied for use in human clinical trials. The identified imaging biomarkers can advance the development of new treatments for SCI that can target longitudinal pathological symptoms of SCI and improve long-term recovery prognosis for SCI patients.

## 5 | Conclusion

Multi-parametric MR imaging metrics of structural myelination (qMT PSR) and neuroinflammation (CEST APT) changes after spinal cord injury are sensitive indicators of injury severity, correlate with behavioral deficits, and report recovery progression after injury. Both imaging metrics reliably reflected the effects of the administration of the neuroprotective drug riluzole and may be used as biomarkers of the effects of other drugs.

---

### Acknowledgments

The authors gratefully acknowledge Zou Yue and Chaohui Tang for their assistance with surgical procedures and perfusion of animals, the Center for Small Animal Imaging (CSAI) staff for imaging support, and the Vanderbilt University Medical Center (VUMC) Translational Pathology Shared Resource Core (NCI/NIH Cancer Center Support Grant 2P30 CA068485-14) for their expertise with processing the spinal cord tissue histology.

### Data Availability Statement

The data that support the findings of this study are available from the corresponding author upon reasonable request.

### References

1. K. M. Mehdar, A. A. Mahjri, A. A. Al Rashah, and A. Alyazidi, "Epidemiology of Spinal Cord Injuries and Their Outcomes: A Retrospective Study at the King Khalid Hospital," *Cureus* 11, no. 12 (2019), <https://doi.org/10.7759/CUREUS.6511>.
2. R. Sweis and J. Biller, "Systemic Complications of Spinal Cord Injury," *Current Neurology and Neuroscience Reports* 17, no. 2 (2017): 1–8, <https://doi.org/10.1007/s11910-017-0715-4>.
3. D. J. Strauss, M. J. DeVivo, D. R. Paculdo, and R. M. Shavelle, "Trends in Life Expectancy After Spinal Cord Injury," *Archives of Physical Medicine and Rehabilitation* 87, no. 8 (2006): 1079–1085, <https://doi.org/10.1016/J.APMR.2006.04.022>.
4. R. M. Shavelle, M. J. Devivo, J. C. Brooks, D. J. Strauss, and D. R. Paculdo, "Improvements in Long-Term Survival After Spinal Cord Injury?," *Archives of Physical Medicine and Rehabilitation* 96, no. 4 (2015): 645–651, <https://doi.org/10.1016/J.APMR.2014.11.003>.
5. A. T. Stammers, J. Liu, and B. K. Kwon, "Expression of Inflammatory Cytokines Following Acute Spinal Cord Injury in a Rodent Model," *Journal of Neuroscience Research* 90, no. 4 (2012): 782–790, <https://doi.org/10.1002/JNR.22820>.

6. M. B. Orr and J. C. Gensel, "Spinal Cord Injury Scarring and Inflammation: Therapies Targeting Glial and Inflammatory Responses," *Neurotherapeutics* 15, no. 3 (2018): 541–553, <https://doi.org/10.1007/S13311-018-0631-6>.
7. T. Zrzavy, C. Schwaiger, I. Wimmer, et al., "Acute and non-resolving Inflammation Associate With Oxidative Injury After Human Spinal Cord Injury," *Brain* 144, no. 1 (2021): 144–161, <https://doi.org/10.1093/BRAIN/AWAA360>.
8. J. W. Fawcett and R. A. Asher, "The Glial Scar and Central Nervous System Repair," *Brain Research Bulletin* 49, no. 6 (1999): 377–391, [https://doi.org/10.1016/S0361-9230\(99\)00072-6](https://doi.org/10.1016/S0361-9230(99)00072-6).
9. G. Yiu and Z. He, "Glial Inhibition of CNS Axon Regeneration," *Nature Reviews. Neuroscience* 7, no. 8 (2006): 617–627, <https://doi.org/10.1038/nrn1956>.
10. Y. S. Gwak and C. E. Hulsebosch, "GABA and Central Neuropathic Pain Following Spinal Cord Injury," *Neuropharmacology* 60, no. 5 (2011): 799–808, <https://doi.org/10.1016/J.NEUROPHARM.2010.12.030>.
11. V. Failli, M. A. Kopp, C. Gericke, et al., "Functional Neurological Recovery After Spinal Cord Injury Is Impaired in Patients With Infections," *Brain* 135, no. 11 (2012): 3238–3250, <https://doi.org/10.1093/BRAIN/AWS267>.
12. M. O. Totoiu and H. S. Keirstead, "Spinal Cord Injury Is Accompanied by Chronic Progressive Demyelination," *Journal of Comparative Neurology* 486, no. 4 (2005): 373–383, <https://doi.org/10.1002/CNE.20517>.
13. A. Alizadeh, S. M. Dyck, and S. Karimi-Abdolrezaee, "Traumatic Spinal Cord Injury: An Overview of Pathophysiology, Models and Acute Injury Mechanisms," *Frontiers in Neurology* 10 (2019): 282, <https://doi.org/10.3389/fneur.2019.00282>.
14. V. Neirinckx, C. Coste, R. Franzen, A. Gothot, B. Rogister, and S. Wislet, "Neutrophil Contribution to Spinal Cord Injury and Repair," *Journal of Neuroinflammation* 11, no. 1 (2014): 1–9, <https://doi.org/10.1186/S12974-014-0150-2>.
15. A. Buss, G. A. Brook, and B. Kakulas, "Gradual Loss of Myelin and Formation of an Astrocytic Scar During Wallerian Degeneration in the Human Spinal Cord," *Brain* 127, no. 1 (2004): 34–44, <https://doi.org/10.1093/BRAIN/AWH001>.
16. E. Park, A. A. Velumian, and M. G. Fehlings, "The Role of Excitotoxicity in Secondary Mechanisms of Spinal Cord Injury: A Review With an Emphasis on the Implications for White Matter Degeneration," *Journal of Neurotrauma* 21, no. 6 (2004): 754–774, <https://doi.org/10.1089/0897715041269641>.
17. F. Papastefanaki and R. Matsas, "From Demyelination to Remyelination: The Road Toward Therapies for Spinal Cord Injury," *Glia* 63, no. 7 (2015): 1101–1125, <https://doi.org/10.1002/GLIA.22809>.
18. J. H. Badhiwala, C. S. Ahuja, and M. G. Fehlings, "Time Is Spine: A Review of Translational Advances in Spinal Cord Injury," *Journal of Neurosurgery. Spine* 30, no. 1 (2019): 1–18, <https://doi.org/10.3171/2018.9.SPINE18682>.
19. P. C. M. Van Zijl and N. N. Yadav, "Chemical Exchange Saturation Transfer (CEST): What Is in a Name and What Isn't?," *Magnetic Resonance in Medicine* 65, no. 4 (2011): 927–948, <https://doi.org/10.1002/MRM.22761>.
20. S. By, R. L. Barry, A. K. Smith, et al., "Amide Proton Transfer CEST of the Cervical Spinal Cord in Multiple Sclerosis Patients at 3T," *Magnetic Resonance in Medicine* 79, no. 2 (2018): 806–814, <https://doi.org/10.1002/MRM.26736>.
21. F. Kogan, A. Singh, C. Debrosse, et al., "Imaging of Glutamate in the Spinal Cord Using GluCEST," *NeuroImage* 77 (2013): 262–267, <https://doi.org/10.1016/j.neuroimage.2013.03.072>.
22. C. Mu, J. L. Reed, F. Wang, M. N. Tantawy, J. C. Gore, and L. M. Chen, "Spatiotemporal Dynamics of Neuroinflammation Relate to Behavioral Recovery in Rats With Spinal Cord Injury," *Molecular Imaging and Biology* 26, no. 2 (2023): 240–252, <https://doi.org/10.1007/S11330-7-023-01875-W>.
23. J. Cohen-Adad, "Microstructural Imaging in the Spinal Cord and Validation Strategies," *NeuroImage* 182 (2018): 169–183, <https://doi.org/10.1016/J.NEUROIMAGE.2018.04.009>.
24. A. K. Smith, R. D. Dortch, L. M. Dethrage, and S. A. Smith, "Rapid, High-Resolution Quantitative Magnetization Transfer MRI of the Human Spinal Cord," *NeuroImage* 95 (2014): 106–116, <https://doi.org/10.1016/J.NEUROIMAGE.2014.03.005>.
25. T. L. Wu, N. E. Byun, F. Wang, et al., "Longitudinal Assessment of Recovery After Spinal Cord Injury With Behavioral Measures and Diffusion, Quantitative Magnetization Transfer and Functional Magnetic Resonance Imaging," *NMR in Biomedicine* 33, no. 4 (2020): e4216, <https://doi.org/10.1002/NBM.4216>.
26. F. Wang, K. Li, A. Mishra, D. Gochberg, L. Min Chen, and J. C. Gore, "Longitudinal Assessment of Spinal Cord Injuries in Nonhuman primates With Quantitative Magnetization Transfer," *Magnetic Resonance in Medicine* 75, no. 4 (2016): 1685–1696, <https://doi.org/10.1002/mrm.25725s>.
27. F. Wang, T. L. Wu, K. Li, L. M. Chen, and J. C. Gore, "Spatiotemporal Trajectories of Quantitative Magnetization Transfer Measurements in Injured Spinal Cord Using Simplified Acquisitions," *NeuroImage: Clinical* 23 (2019): 101921, <https://doi.org/10.1016/J.NICL.2019.101921>.
28. N. Nagoshi, H. Nakashima, and M. Fehlings, "Riluzole as a Neuroprotective Drug for Spinal Cord Injury: From Bench to Bedside," *Molecules* 20, no. 5 (2015): 7775–7789, <https://doi.org/10.3390/molecules20057775>.
29. M. G. Fehlings, J. R. Wilson, R. F. Frankowski, et al., "Riluzole for the Treatment of Acute Traumatic Spinal Cord Injury: Rationale for and Design of the NACTN Phase I Clinical Trial," *Journal of Neurosurgery. Spine* 17, no. Suppl1 (2012): 151–156, <https://doi.org/10.3171/2012.4.AOSPINE1259>.
30. Y. Wu, K. Satkunendrarajah, Y. Teng, D. S. L. Chow, J. Buttigieg, and M. G. Fehlings, "Delayed Post-Injury Administration of Riluzole Is Neuroprotective in a Preclinical Rodent Model of Cervical Spinal Cord Injury," *Journal of Neurotrauma* 30, no. 6 (2013): 441–452, <https://doi.org/10.1089/neu.2012.2622>.
31. M. Lu, G. Drake, F. Wang, et al., "Design and Construction of an Interchangeable RF Coil System for Rodent Spinal Cord MR Imaging at 9.4 T," *Magnetic Resonance Imaging* 84 (2021): 124–131, <https://doi.org/10.1016/j.mri.2021.09.015>.
32. A. Ramani, C. Dalton, D. H. Miller, P. S. Tofts, and G. J. Barker, "Precise Estimate of Fundamental in-Vivo MT Parameters in Human Brain in Clinically Feasible Times," *Magnetic Resonance Imaging* 20, no. 10 (2002): 721–731, [https://doi.org/10.1016/S0730-725X\(02\)00598-2](https://doi.org/10.1016/S0730-725X(02)00598-2).
33. F. Heath, S. A. Hurley, H. Johansen-Berg, and C. Sampaio-Baptista, "Advances in Noninvasive Myelin Imaging," *Developmental Neurobiology* 78, no. 2 (2018): 136–151, <https://doi.org/10.1002/dneu.22552>.
34. T. O'Haver, "peakfit.m," accessed July 1, 2022, <https://www.mathworks.com/matlabcentral/fileexchange/23611-peakfit-m>.
35. D. M. Basso, M. S. Beattie, and J. C. Bresnahan, "A Sensitive and Reliable Locomotor Rating Scale for Open Field Testing in Rats," *Journal of Neurotrauma* 12, no. 1 (1995): 1–21, <https://doi.org/10.1089/neu.1995.12.1>.
36. N. D. Jeffery, K. Brakel, M. Aceves, M. A. Hook, and U. B. Jeffery, "Variability in Open-Field Locomotor Scoring Following Force-Defined Spinal Cord Injury in Rats: Quantification and Implications," *Frontiers in Neurology* 11 (2020): 650, <https://doi.org/10.3389/fneur.2020.00650>.
37. A. D. Kloos, L. C. Fisher, M. R. Detloff, D. L. Hassenzahn, and D. M. Basso, "Stepwise Motor and All-or-None Sensory Recovery Is Associated With Nonlinear Sparing After Incremental Spinal Cord Injury in Rats," *Experimental Neurology* 191, no. 2 (2005): 251–265, <https://doi.org/10.1016/J.EXPNEUROL.2004.09.016>.

38. J. R. Deuis, L. S. Dvorakova, and I. Vetter, "Methods Used to Evaluate Pain Behaviors in Rodents," *Frontiers in Molecular Neuroscience* 10 (2017): 284, <https://doi.org/10.3389/fnmol.2017.00284>.
39. Z. Ahmed, G. Shaw, V. P. Sharma, C. Yang, E. McGowan, and D. W. Dickson, "Actin-Binding Proteins Coronin-1a and IBA-1 Are Effective Microglial Markers for Immunohistochemistry," *Journal of Histochemistry and Cytochemistry* 55, no. 7 (2007): 687–700, <https://doi.org/10.1369/jhc.6A7156.2007>.
40. L. F. Eng, "Glial Fibrillary Acidic Protein (GFAP): The Major Protein of Glial Intermediate Filaments in Differentiated Astrocytes," *Journal of Neuroimmunology* 8, no. C (1985): 203–214, [https://doi.org/10.1016/S0165-5728\(85\)80063-1](https://doi.org/10.1016/S0165-5728(85)80063-1).
41. C. L. Scholtz, "Quantitative Histochemistry of Myelin Using Luxol Fast Blue MBS," *Histochemical Journal* 9, no. 6 (1977): 759–765, <https://doi.org/10.1007/BF01003070>.
42. P. Bankhead, M. B. Loughrey, J. A. Fernández, et al., "QuPath: Open Source Software for Digital Pathology Image Analysis," *Scientific Reports* 71, no. 1 (2017): 1–7, 7, <https://doi.org/10.1038/s41598-017-17204-5>.
43. M. Rausch, P. S. Tofts, P. Lervik, et al., "Characterization of White Matter Damage in Animal Models of Multiple Sclerosis by Magnetization Transfer Ratio and Quantitative Mapping of the Apparent Bound Proton Fraction f\*," *Multiple Sclerosis* 15, no. 1 (2009): 16–27, <https://doi.org/10.1177/1352458508096006>.
44. A. K. Smith, S. By, B. D. Lyttle, et al., "Evaluating Single-Point Quantitative Magnetization Transfer in the Cervical Spinal Cord: Application to Multiple Sclerosis," *NeuroImage: Clinical* 16 (2017): 58–65, <https://doi.org/10.1016/J.NICL.2017.07.010>.
45. H. R. Underhill, R. C. Rostomily, A. M. Mikheev, C. Yuan, and V. L. Yarnykh, "Fast Bound Pool Fraction Imaging of the In Vivo rat Brain: Association With Myelin Content and Validation in the C6 Glioma Model," *NeuroImage* 54, no. 3 (2011): 2052–2065, <https://doi.org/10.1016/J.NEUROIMAGE.2010.10.065>.
46. J. Zhou, H. Y. Heo, L. Knutsson, P. C. M. van Zijl, and S. Jiang, "APT-Weighted MRI: Techniques, Current Neuro Applications, and Challenging Issues," *Journal of Magnetic Resonance Imaging* 50, no. 2 (2019): 347–364, <https://doi.org/10.1002/JMRI.26645>.
47. H. Zhang, W. Wang, S. Jiang, et al., "Amide Proton Transfer-Weighted MRI Detection of Traumatic Brain Injury in Rats," *Journal of Cerebral Blood Flow and Metabolism* 37, no. 10 (2017): 3422–3432, <https://doi.org/10.1177/0271678X17690165>.
48. A. Tietze, J. Blicher, I. K. Mikkelsen, et al., "Assessment of Ischemic Penumbra in Patients With Hyperacute Stroke Using Amide Proton Transfer (APT) Chemical Exchange Saturation Transfer (CEST) MRI," *NMR in Biomedicine* 27, no. 2 (2014): 163–174, <https://doi.org/10.1002/nbm.3048>.
49. L. M. Chen, F. Wang, A. Mishra, et al., "Longitudinal Multiparametric MRI of Traumatic Spinal Cord Injury in Animal Models," *Magnetic Resonance Imaging* 102 (2023): 184–200, <https://doi.org/10.1016/J.MRI.2023.06.007>.
50. W. Wang, H. Zhang, D. H. Lee, et al., "Using Functional and Molecular MRI Techniques to Detect Neuroinflammation and Neuroprotection After Traumatic Brain Injury," *Brain, Behavior, and Immunity* 64 (2017): 344–353, <https://doi.org/10.1016/J.BBI.2017.04.019>.